EUROPEAN ORGANIZATION FOR NUCLEAR RESEARCH (CERN)

CERN-EP-2021-143
2022/05/16

CMS-TOP-18-007

Search for CP violating top quark couplings in pp collisions at $\sqrt{s} = 13\,\text{TeV}$

The CMS Collaboration

Abstract

Results are presented from a search for CP violation in top quark pair production, using proton-proton collisions at a center-of-mass energy of 13 TeV. The data used for this analysis consist of final states with two charged leptons collected by the CMS experiment, and correspond to an integrated luminosity of 35.9 fb^{-1}. The search uses two observables, $\mathcal{O}_1$ and $\mathcal{O}_3$, which are Lorentz scalars. The observable $\mathcal{O}_1$ is constructed from the four-momenta of the charged leptons and the reconstructed top quarks, while $\mathcal{O}_3$ consists of the four-momenta of the charged leptons and the b quarks originating from the top quarks. Asymmetries in these observables are sensitive to CP violation, and their measurement is used to determine the chromoelectric dipole moment of the top quark. The results are consistent with the expectation from the standard model.

Submitted to the Journal of High Energy Physics

1 Introduction

The combination of charge conjugation and parity transformation (CP) is a symmetry known to be violated in the standard model (SM). CP violation was initially observed in kaon decays [1]. Many experiments have studied CP violation in other processes for the last three decades [2–4]. However, the magnitude of CP violation observed so far is not enough to accommodate the matter-antimatter asymmetry in the universe [5, 6], motivating searches for additional CP violation.

It has been proposed that CP violation also takes place in the production and decay of top quark pairs ($\mathrm{t\bar{t}}$) [7, 8]. Several models predict CP violations, including the multi-Higgs-doublet model and the minimal supersymmetric SM; in the 1st model, for example, the exchanges of neutral and charged Higgs bosons can generate dipole moments from the top quark. In the SM, only a very small amount of CP violation is expected to occur at the production vertex, as this requires at least three loops [7, 8]. If a non-zero chromoelectric dipole moment (CEDM) is observed at the $\mathrm{t\bar{t}}$ production vertex and the top quarks decay into Wb following the SM process, this can be a signal of CP violation in top quark pair events.

The flavor-diagonal dipole couplings between top quarks and gluons of magnetic and electric origin would be defined through a Lagrangian density

$$\mathcal{L} = \frac{g_\mathrm{S}}{2}\bar{\mathrm{t}}T^a\sigma^{\mu\nu}(a_\mathrm{t}^\mathrm{g} + i\gamma_5\frac{\sqrt{2}v}{\Lambda^2}\mathrm{Im}(d_{\mathrm{t}G}))\mathrm{t}G^a_{\mu\nu}, \tag{1}$$

where $\mathrm{Im}(d_{\mathrm{t}G})$ is the CP-odd CEDM, and a_t^g, g_S, T^a, and $G_{\mu\nu}$ represent the chromomagnetic dipole moment, the strong coupling ($g_\mathrm{S} = \sqrt{4\pi\alpha_\mathrm{S}}$), Gell-Mann matrices, and the field strength tensor, respectively. The scale Λ is the scale of the new physics responsible for the CP violation of CEDM, and $v \approx 246\,\mathrm{GeV}$ is the vacuum expectation value of the Higgs field. The discussion in Ref. [8] introduces various observables that probe such CP violation effects.

The studies presented in this analysis define two observables with CP-odd correlation in $\mathrm{t\bar{t}}$ events in the dilepton final state, where both W bosons decay leptonically:

$$\mathcal{O}_1 = \epsilon(p_\mathrm{t}, p_{\bar{\mathrm{t}}}, p_{\ell+}, p_{\ell-}) = \begin{vmatrix} E_\mathrm{t} & p_{\mathrm{t},x} & p_{\mathrm{t},y} & p_{\mathrm{t},z} \\ E_{\bar{\mathrm{t}}} & p_{\bar{\mathrm{t}},x} & p_{\bar{\mathrm{t}},y} & p_{\bar{\mathrm{t}},z} \\ E_{\ell+} & p_{\ell+,x} & p_{\ell+,y} & p_{\ell+,z} \\ E_{\ell-} & p_{\ell-,x} & p_{\ell-,y} & p_{\ell-,z} \end{vmatrix}, \tag{2}$$

and

$$\mathcal{O}_3 = \epsilon(p_\mathrm{b}, p_{\bar{\mathrm{b}}}, p_{\ell+}, p_{\ell-}) = \begin{vmatrix} E_\mathrm{b} & p_{\mathrm{b},x} & p_{\mathrm{b},y} & p_{\mathrm{b},z} \\ E_{\bar{\mathrm{b}}} & p_{\bar{\mathrm{b}},x} & p_{\bar{\mathrm{b}},y} & p_{\bar{\mathrm{b}},z} \\ E_{\ell+} & p_{\ell+,x} & p_{\ell+,y} & p_{\ell+,z} \\ E_{\ell-} & p_{\ell-,x} & p_{\ell-,y} & p_{\ell-,z} \end{vmatrix}. \tag{3}$$

These observables are obtained contracting the Levi-Civita tensor ϵ [8] with four 4-momenta, which results in the determinant of a 4×4 matrix. The components of $\mathcal{O}_1$ and $\mathcal{O}_3$ are the four-momenta p of the charged leptons ($\ell^\pm$), the reconstructed top quarks and antiquarks, and the b quark and antiquark jets. The elements in the 4×4 matrices are therefore the energy E and three-momentum components p_x, p_y, p_z of these objects. Since these observables are scalars under Lorentz transformations, they do not depend on the reference frame.

The observables $\mathcal{O}_1$ and $\mathcal{O}_3$ are odd under the CP transformation. Hence, CP violation in the production of $\mathrm{t\bar{t}}$ can be tested by a measurement of the asymmetries A_i of the number of

produced events, N, with a positive and negative value in the observable $\mathcal{O}_i$:

$$A_i = \frac{N(\mathcal{O}_i > 0) - N(\mathcal{O}_i < 0)}{N(\mathcal{O}_i > 0) + N(\mathcal{O}_i < 0)}. \quad (4)$$

As argued in Ref. [8], the asymmetries of $\mathcal{O}_1$ and $\mathcal{O}_3$ are the observables with highest sensitivity to CP violation, and are linearly correlated to d_{tG}. While the lack of a sizable asymmetry in $t\bar{t}$ production and decay would be consistent with the SM, a significant nonzero asymmetry would indicate the existence of CP violation and hence, new physics [9, 10]. In certain models predicting a CEDM (see Ref. [8]), the asymmetries in $\mathcal{O}_1$ and $\mathcal{O}_3$ can be as large as 15 and 9%, respectively. Asymmetries have been measured by the CMS Collaboration at $\sqrt{s} = 8$ TeV in the lepton+jets channel [11]. In this paper the asymmetries of the observables $\mathcal{O}_1$ and $\mathcal{O}_3$ measured in the dilepton channel at 13 TeV, as well as the $\mathrm{Im}(d_{tG})$ derived from those asymmetries, are presented. The tabulated results are provided in HEPData [12].

2 The CMS Detector

The central feature of the CMS apparatus is a superconducting solenoid of 6 m internal diameter, providing a magnetic field of 3.8 T. Within the solenoid volume are a silicon pixel and strip tracker, a lead tungstate crystal electromagnetic calorimeter (ECAL), and a brass and scintillator hadron calorimeter, each composed of a barrel and two endcap sections. Forward calorimeters extend the pseudorapidity (η) coverage provided by the barrel and endcap detectors. Muons are detected in gas-ionization chambers embedded in the steel flux-return yoke outside the solenoid. Events of interest are selected using a two-tiered trigger system [13]. The first level, composed of custom hardware processors, uses information from the calorimeters and muon detectors to select events at a rate of around 100 kHz within a fixed time interval of less than 4 μs. The second level, known as the high-level trigger, consists of a farm of processors running a version of the full event reconstruction software optimized for fast processing, and reduces the event rate to around 1 kHz before data storage. A more detailed description of the CMS detector, together with a definition of the coordinate system used and the relevant kinematic variables, can be found in Ref. [14].

3 Simulated events

The $t\bar{t}$ event candidates in the dilepton final state are selected and compared with simulated events to investigate the composition of processes in the data.

Simulated $t\bar{t}$ events are generated at next-to-leading order (NLO) using the POWHEG generator (v. 2) [15–21] at a top quark mass (m_t) of 172.5 GeV. The events are simulated with PYTHIA (v. 8.219) [22], referred to as PYTHIA 8 in the following, to simulate parton showers (PS) and hadronization using the underlying-event (UE) tune CUETP8M2 [23]. The NNPDF3.0 parton distribution function (PDF) set is used to describe the proton structure. In this analysis, $t\bar{t}$ events with two oppositely charged leptons (e^+e^-, $e^\pm\mu^\mp$, and $\mu^+\mu^-$) originating from W boson decays are considered as signal ("$t\bar{t}$ signal"). All other $t\bar{t}$ events ($t\bar{t}$ originating from leptonic decays of τ leptons, all-jet final states, or lepton+jet events) are regarded as a background (referred to as "$t\bar{t}$ other"). The impact of not including the events where charged leptons originate from τ decays as "$t\bar{t}$ signal" is small since the information contained in the lepton from a τ decay is diluted relative to the τ lepton.

Drell–Yan ($q\bar{q} \to Z^*/\gamma \to \ell^+\ell^-$, referred to as DY), W+jets, WW, WZ, ZZ, $t\bar{t}$+W, $t\bar{t}$+Z, and the tW channel of single top quark production regarded as the processes that can have similar

decay topologies to $t\bar{t}$ in the dilepton final state. The DY process is simulated with up to four additional partons at leading-order (LO) precision using the MADGRAPH5_aMC@NLO event generator (v. 2.2.2) with the MLM jet merging prescription [24] and the CUETP8M1 tune [25]. The $t\bar{t}$+V (where V refers to a W or Z) processes are simulated using MADGRAPH5_aMC@NLO, with PYTHIA 8 for parton showering and hadronization, and the CUETP8M1 tune. Events from WW, WZ, and ZZ diboson processes are generated at LO using PYTHIA 8 and the CUETP8M1 tune. The tW channel is simulated with POWHEG (v. 1) interfaced to PYTHIA 8 using the UE tune CUETP8M2T4. The W+jets events are generated at NLO using MADGRAPH5_aMC@NLO and interfaced to PYTHIA 8 with the UE tune CUETP8M1.

The interactions of particles within the CMS detector are modeled using the detector simulation GEANT4 [26].

To model the effect of additional pp interactions within the same or nearby bunch crossing (pileup), simulated minimum-bias interactions are inserted into the simulated events. The distribution of pileup in simulation is matched to the observed data by reweighting the simulated pileup distributions, assuming a total inelastic pp cross section of 69.2 mb [27].

The simulations are normalized to the theoretical cross sections and the integrated luminosity of the data. The cross sections for the DY and W+jets processes are normalized to their next-to-NLO (NNLO) prediction obtained from the FEWZ framework (v. 3.1.b2) [28]. Single top quark production is normalized to the approximate NNLO prediction [29], and diboson and $t\bar{t}$+V processes to the NLO prediction [30–32]. The $t\bar{t}$ cross section, computed at NNLO with a next-to-next-to-leading logarithmic (NNLL) accuracy for soft gluon resummation, is $832^{+20}_{-29}\,(\text{scale}) \pm 35\,(\text{PDF}+\alpha_S)$ pb, where the scale uncertainty comes from varying the normalization and factorization scales and the PDF+α_S uncertainly is obtained from different PDF sets and varying α_S [33].

4 Event reconstruction and selection

The data used for this analysis are from proton-proton (pp) collisions collected at $\sqrt{s} = 13$ TeV in the CMS detector, and correspond to an integrated luminosity of 35.9 fb^{-1}. The event selection is optimized to select $t\bar{t}$ events in which both top quarks decay to a leptonically decaying W boson.

The events are further selected and categorized into channels by lepton flavor (e^+e^-, $e^\pm\mu^\mp$, and $\mu^+\mu^-$). The selected events are required to pass a combination of single-lepton and dilepton triggers. In each event, at least one of the following triggers must be satisfied. The single-lepton trigger requires at least one isolated electron or muon with a transverse momentum $p_T > 27$ or 24 GeV and with $|\eta| < 2.4$, respectively. The same-flavor dilepton triggers require a leading-p_T lepton with $p_T > 23$ or 17 GeV, and a subleading-p_T lepton with $p_T > 12$ or 8 GeV. The different-flavor dilepton triggers require either an electron with $p_T > 12$ GeV and a muon with $p_T > 23$ GeV, or an electron with $p_T > 23$ GeV and a muon with $p_T > 8$ GeV.

The selected events are reconstructed offline using a particle-flow (PF) algorithm [34] that aims to reconstruct and identify each individual particle (PF candidate) in an event, with an optimized combination of information from the various elements of the CMS detector.

Electron candidates are reconstructed using tracking and ECAL information [35] and are excluded when their ECAL clusters are located in the transition region between the barrel and endcap detectors ($1.4442 < |\eta| < 1.5660$) because the reconstruction efficiency in this region is reduced. A relative isolation criterion $I_{\text{rel}} < 0.0588$ (0.0571) is applied for an electron candi-

date in the barrel (endcap), where the I_{rel} is defined as the p_{T} sum of all neutral and, charged hadron, and photon candidates within a distance $\Delta R = \sqrt{(\Delta\eta)^2 + (\Delta\phi)^2} = 0.3$ (where ϕ is the azimuthal angle in radians) from the electron candidate in η–ϕ space, divided by the p_{T} of the electron candidate, with a correction that suppresses the residual effect of pileup collisions [36]. In addition, electron identification requirements are applied to reject misidentified electron candidates and candidates originating from photon conversions. The electron candidates must have $p_{\text{T}} > 25$ and 20 GeV for the leading and subleading candidate, respectively, within $|\eta| < 2.4$.

Muon candidates are reconstructed from the track information in the tracker and muon system [37]. They must be in the same p_{T} and $|\eta|$ ranges as the electron candidates above.

A relative isolation requirement of $I_{\text{rel}} < 0.15$ is applied to muon candidates and lie within $\Delta R = 0.4$ of the muon in η–ϕ space. In addition, muon identification requirements are used to reject muon candidates that are misidentified hadrons or come from the decay of charged pions or kaons [37].

Jets are reconstructed by clustering the PF candidates using the anti-k_{T} algorithm with a distance parameter $R = 0.4$ [38, 39]. The momentum of the jet is defined as the vector sum of all particle momenta in the jet cone, and is found from simulation to be within 5 to 10% of the true momentum over the entire p_{T} range of interest and detector acceptance. Since pileup collisions contribute calorimetric energy depositions and extra tracks, tracks identified as originating from pileup vertices are discarded [34]. In addition, an offset correction is applied to jet energies in order to remove the residual energy contribution from pileup [40]. The energy scale corrections of jets are obtained from simulation and used to bring the mean measured response to that of jets at particle level. In situ measurements of the momentum imbalance in dijet, photon+jets, Z+jets, and multijet events are used to account for any residual differences between jet energy in data and simulation [40]. Jets are required to have $p_{\text{T}} > 30$ GeV and $|\eta| < 2.4$. If the separation ΔR between the jet and the closest lepton is <0.4, the jet is discarded.

Jets originating from the fragmentation and hadronization of b quarks are identified ("b tagged") using the combined secondary vertex algorithm that uses information from track impact parameters and secondary vertices identified within a given jet. The chosen working point provides a b jet identification efficiency of approximately 63% with a probability to misidentify light-flavor jets as b jets of $\approx$1% in $\mathrm{t\bar{t}}$ events [41].

The missing transverse momentum vector $\vec{p}_{\text{T}}^{\text{miss}}$ is defined as the projection on the plane perpendicular to the beam axis of the negative vector momenta sum of all reconstructed PF candidates in an event. Its magnitude is referred to as $p_{\text{T}}^{\text{miss}}$.

The selected events are required to have two oppositely charged isolated leptons ($\mathrm{e^+e^-}$, $\mathrm{e^{\pm}\mu^{\mp}}$, or $\mu^+\mu^-$) and at least two jets. At least one of the jets is required to be b tagged. Events with additional loosely isolated electron (muon) of $p_{\text{T}} > 20$ GeV are vetoed. An electron is considered loosely isolated if $I_{\text{rel}} < 0.175$ (barrel) or 0.159 (endcaps). A muon is loosely isolated with $I_{\text{rel}} < 0.25$. The dilepton invariant mass must be greater than 20 GeV to suppress contributions from heavy-flavor resonance decays and low-mass DY events. In same-flavor lepton channels, the backgrounds from Z+jets are further suppressed by rejecting events with a dilepton invariant mass within 76 and 106 GeV (Z boson mass window) and requiring $p_{\text{T}}^{\text{miss}} > 40$ GeV. To estimate the remaining background contribution from Z+jets events in the same-flavor lepton channel, the events outside the Z mass window are normalized to the event yield in simulation within the Z boson mass window. A contamination from non-DY background can be present in the Z boson mass window, and this is taken into account in the estimation in the $\mathrm{e^+e^-}$ and

$\mu^+\mu^-$ channels. These are estimated using the $e^\pm\mu^\mp$ events, which are rescaled, and subtracted in the e^+e^- and $\mu^+\mu^-$ channels. Other sources of background, such as single top quark production, diboson, $t\bar{t}$+V, $t\bar{t}$ other, misidentified leptons, and leptons within jets are estimated using simulations.

Since the observables in Eq. (2) contain the four-momenta of the top quark and antiquark or of the b quark and antiquark, a kinematic event reconstruction [42, 43] is necessary. The algorithm takes into account all combinations of jets and leptons and solves a system of equations based on the following constraints: p_T^{miss} is assumed to originate solely from the two neutrinos; the invariant mass of the reconstructed W boson (m_W) is constrained to 80.4 GeV [44]; and the invariant mass of each reconstructed top quark is constrained to 172.5 GeV. Effects of detector resolution are taken into account through a random smearing of the measured energies and directions of the reconstructed lepton and b jet candidates according to their simulated resolutions. In addition, the assumed invariant mass of the W boson is varied according to the simulated Breit–Wigner distribution of W boson masses [44]. For a given smearing, we choose the solution of the equations for the neutrino momenta yielding the smallest invariant mass of the $t\bar{t}$ system. For each solution, a weight is calculated based on the spectrum of the true invariant mass of the lepton and b jet system from top quark decays at the particle level [43]. The weights are summed over 100 smearings for each combination, and the top quark and antiquark four-momenta are calculated as the weighted average. Among the combinations, we choose the assignment of jets and leptons that yields the maximum sum of weights. The efficiency of the kinematic reconstruction is defined as the fraction of the selected $t\bar{t}$ events where a solution is found, and is about 90% in both data and simulation. Events without solutions for the neutrino momenta are excluded from further analysis. Using this method, the four-momenta of the top quark and antiquark are reconstructed, as are those of the b and $\bar{b}$ quark jets. Event yields for the individual dilepton channels after event selection are shown in Table 1 for the prediction of the $t\bar{t}$ signal, various background processes, and the observed data.

Table 1: Simulated event yields with their statistical uncertainties for the three dilepton channels, after implementing event selection criteria, and normalized as described in the text. Observed selected events are also shown.

Process	e^+e^-	$e^\pm\mu^\mp$	$\mu^+\mu^-$
$t\bar{t}$ signal	$22\,216 \pm 64$	$104\,051 \pm 140$	$45\,818 \pm 93$
$t\bar{t}$ other	$3\,425 \pm 25$	$16\,787 \pm 56$	$7\,502 \pm 38$
Single top quark	899 ± 13	$4\,265 \pm 28$	$1\,793 \pm 18$
DY	700 ± 57	381 ± 26	$1\,627 \pm 95$
$t\bar{t}$+V	72 ± 2	302 ± 4	144 ± 3
Diboson	37 ± 4	100 ± 7	70 ± 6
Total prediction	$27\,350 \pm 90$	$125\,878 \pm 155$	$56\,954 \pm 140$
Data	26 961	126 549	55 993

In Fig. 1, distributions in the observables of the selected leptons and jets are shown for the $e^\pm\mu^\mp$ channel. The events in these distributions satisfy all event selection criteria. Figure 2 shows the p_T distributions of top quark and antiquark reconstructed in the dilepton channel. For each selected event, $\mathcal{O}_1$ and $\mathcal{O}_3$ are computed from the kinematic information of the reconstructed top quarks, b quark jets, and leptons. Figures 3 and 4 present the comparison of data and prediction for the observables $\mathcal{O}_1$ and $\mathcal{O}_3$. In these figures, the values of $\mathcal{O}_1$ and $\mathcal{O}_3$ are divided by the fourth power of m_t to provide better visibility. In Figs. 1–4, the shaded bands in the

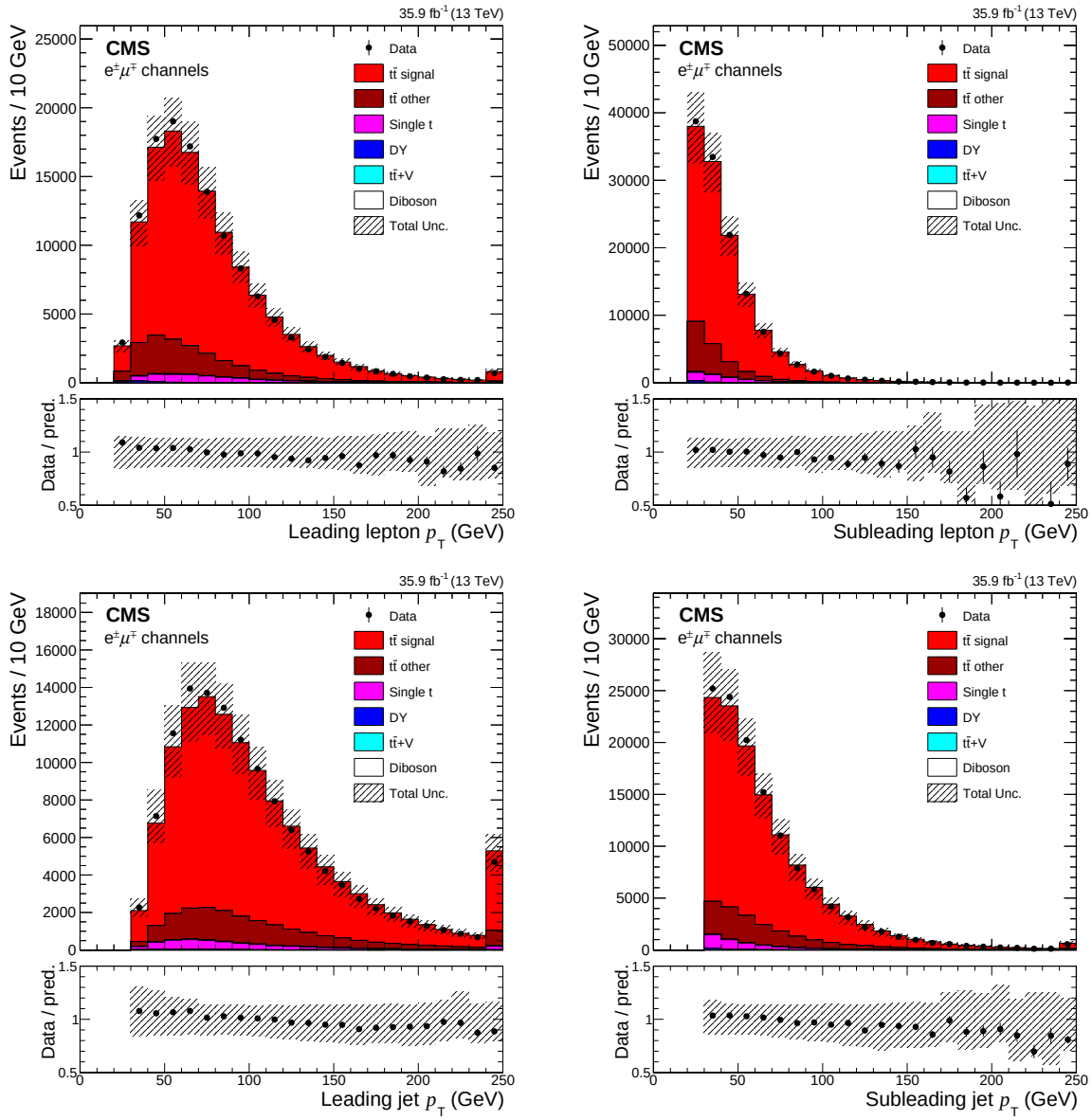

Figure 1: The comparisons of the predictions and observed data in the kinematic distributions of the p_T of the leading lepton (upper left), subleading lepton (upper right), leading jet (lower left), and subleading jet (lower right) in the $e^{\pm}\mu^{\mp}$ channels. The vertical bars on the markers of the observed data represent the statistical uncertainties. The shaded band in the predicted distributions includes statistical and systematic uncertainties. The last bin in each plot includes overflow events. The ratio of the data to the predictions from simulation is presented in the lower panel of each figure.

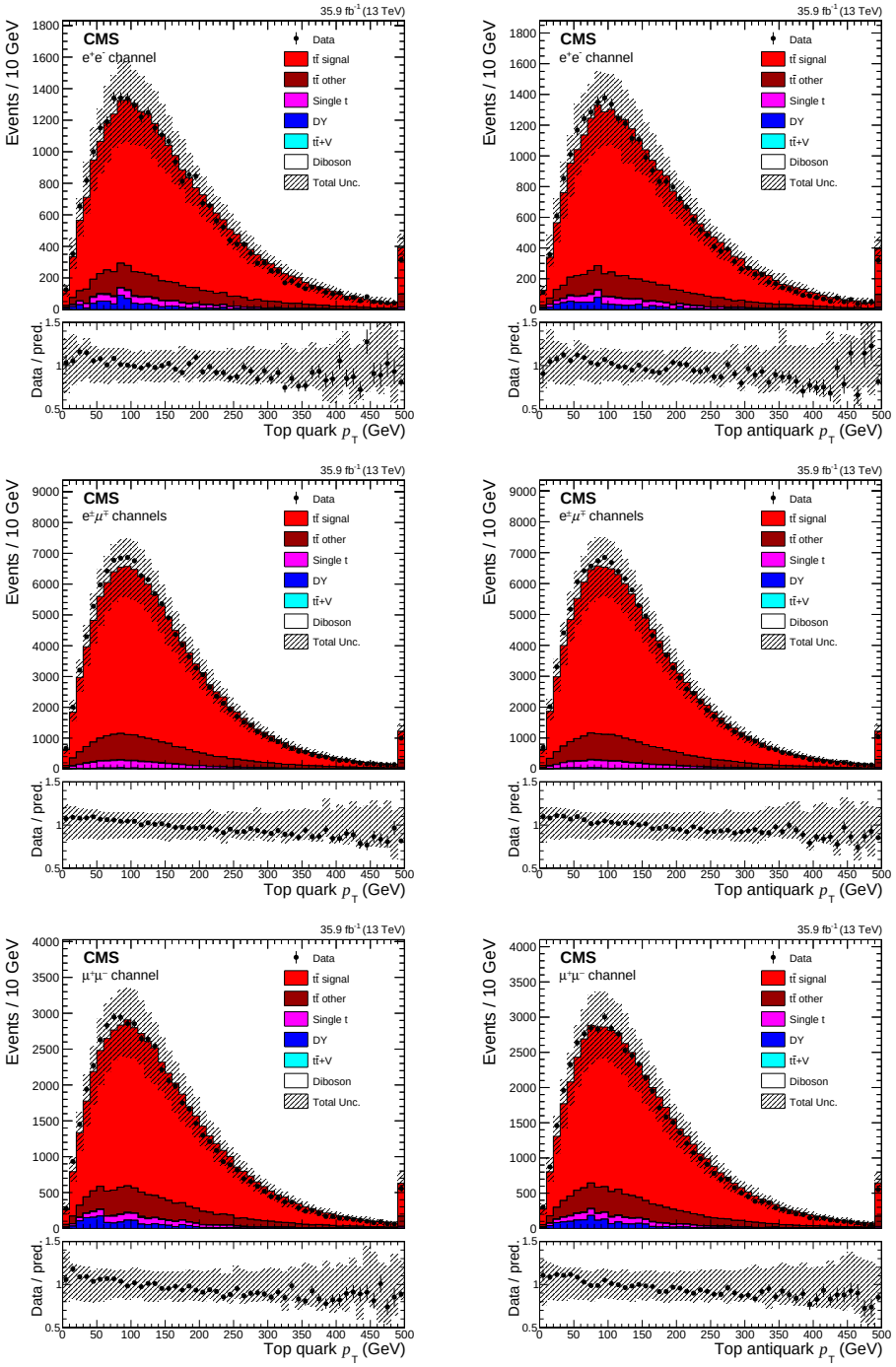

Figure 2: The comparisons of the predictions and observed data in the p_T distributions in the top quark (left) and antiquark (right) in the e^+e^- (upper), $e^\pm\mu^\mp$ (middle) and $\mu^+\mu^-$ (lower) channels. The vertical bars on the markers of the observed data represent the statistical uncertainties. The shaded band in the predicted distributions includes statistical and systematic uncertainties. The last bin in each plot includes overflow events. The ratio of the data to the predictions from simulation is presented in the lower panel of each figure.

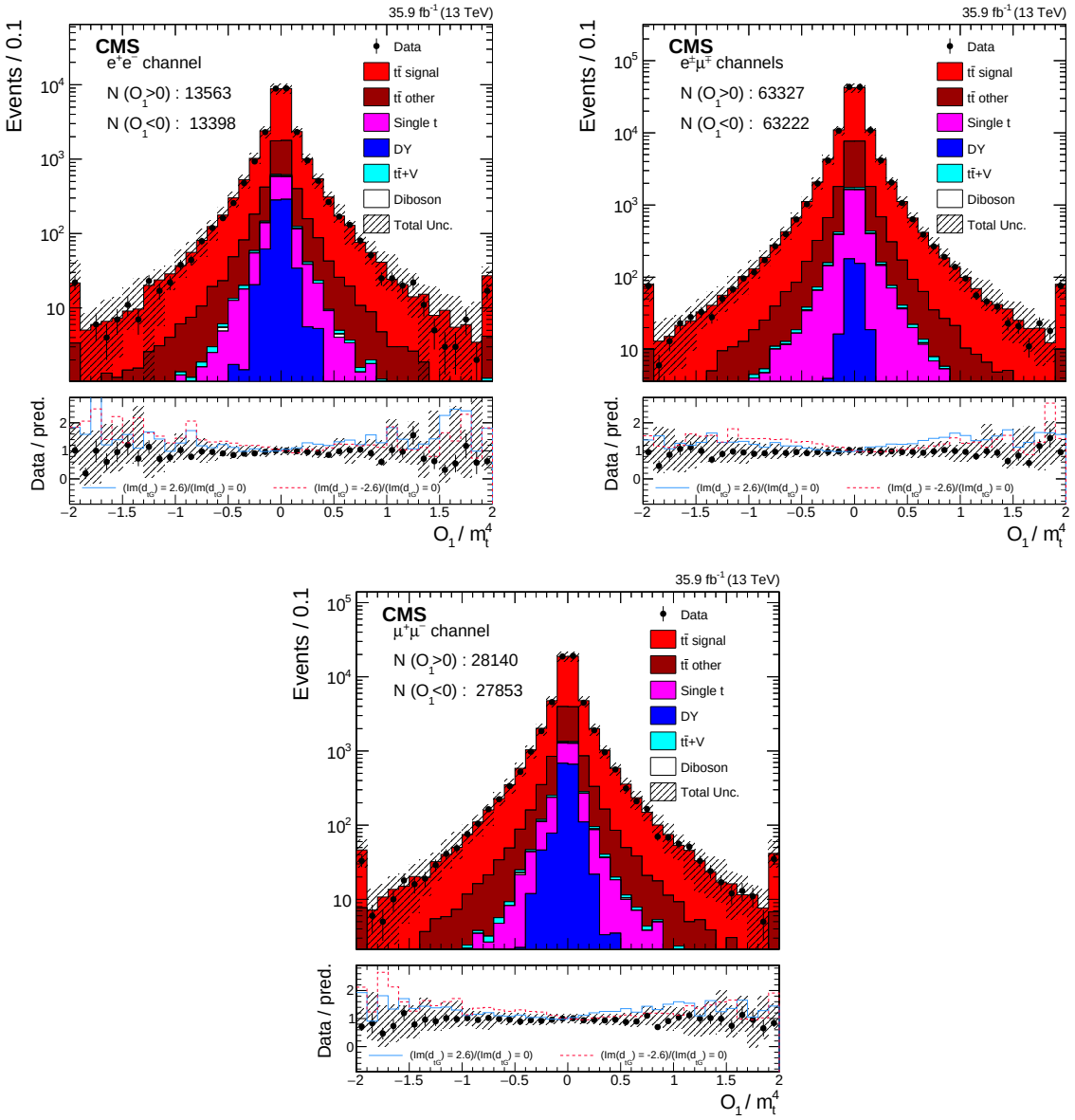

Figure 3: The comparisons of the predictions and observed data in $\mathcal{O}_1$ in the e^+e^- (upper left), $e^{\pm}\mu^{\mp}$ (upper right), and $\mu^+\mu^-$ (lower) channel. The vertical bars on the markers of the observed data represent the statistical uncertainties. The shaded band in the predicted distributions includes statistical and systematic uncertainties. The first and last bins in each plot includes underflow and overflow events, respectively. The ratio of the data to the predictions from simulation is presented in the lower panel of each figure. The solid blue shows the ratio $(\mathrm{Im}(d_{tG}) = 2.6)/(\mathrm{Im}(d_{tG}) = 0)$, and the dashed red line represents the ratio $(\mathrm{Im}(d_{tG}) = -2.6)/(\mathrm{Im}(d_{tG}) = 0)$, using the CEDM samples.

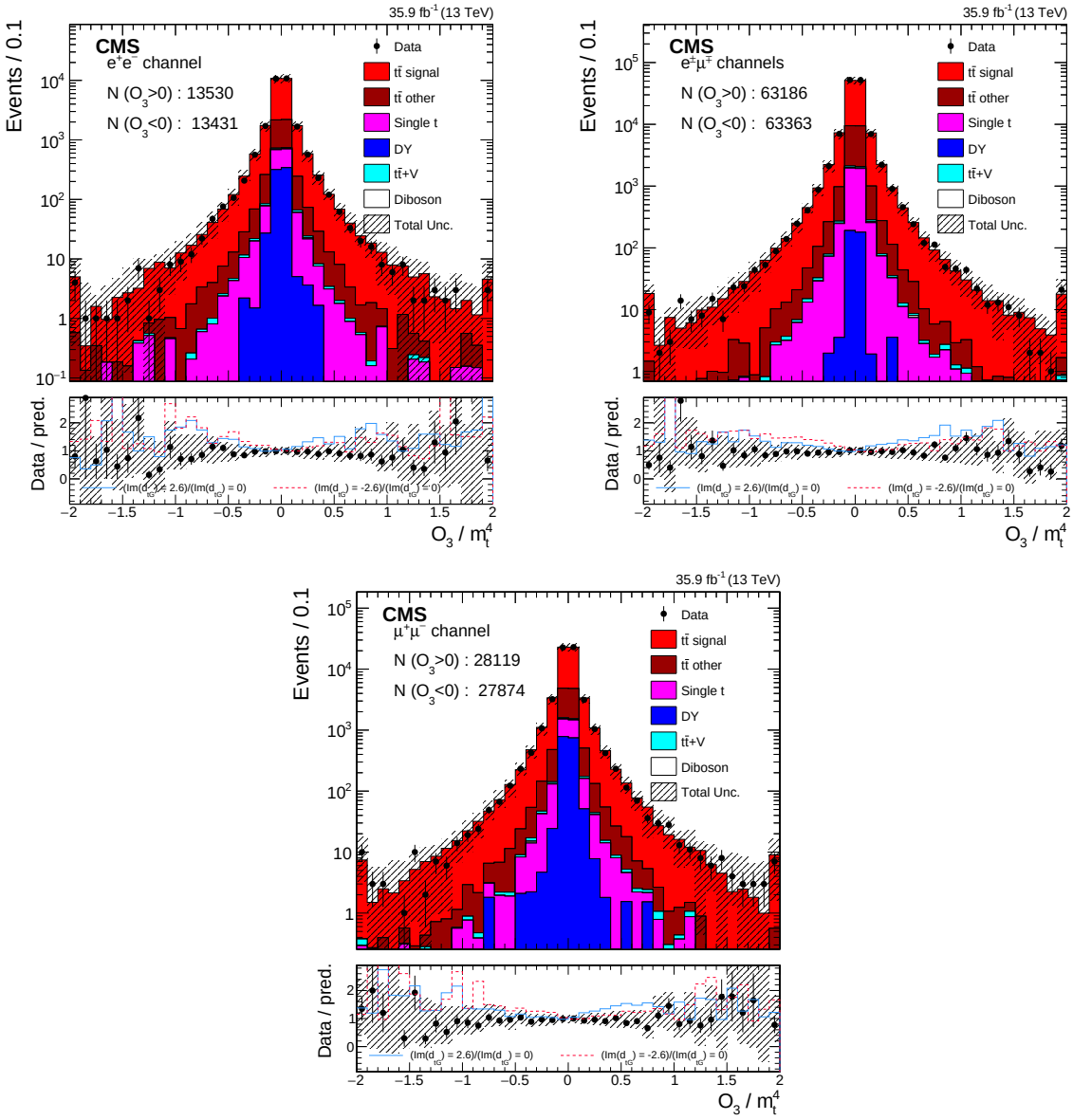

Figure 4: The comparisons of the predictions and observed data in $\mathcal{O}_3$ in the e^+e^- (upper left), $e^{\pm}\mu^{\mp}$ (upper right), and $\mu^+\mu^-$ (lower) channel. The vertical bars on the markers of the observed data represent the statistical uncertainties. The shaded band in the predicted distributions includes statistical and systematic uncertainties. The ratio of the data to the predictions from simulation is presented in the lower panel of each figure. The first and last bins in each plot includes underflow and overflow events, respectively. The solid blue line shows the ratio $(\mathrm{Im}(d_{tG}) = 2.6)/(\mathrm{Im}(d_{tG}) = 0)$, and the dashed red line represents the ratio $(\mathrm{Im}(d_{tG}) = -2.6)/(\mathrm{Im}(d_{tG}) = 0)$, using the CEDM samples.

predicted distributions correspond to the total uncertainty, summing in quadrature the effect of the systematic uncertainties discussed in Section 5.2, and the statistical uncertainties in each bin.

5 Results

5.1 Extraction of asymmetries

The distributions in Figs. 3 and 4 are split into positive and negative regions based on the algebraic sign of the observable. The corresponding Poisson probability density functions for the observed and predicted numbers of events is used to construct a likelihood function that essentially reflects Eq. (4). Using a maximum likelihood fit, the asymmetry A_i of the observable $\mathcal{O}_i$ and the $\mathrm{t\bar{t}}$ production cross section, $\sigma_{\mathrm{t\bar{t}}}$, are extracted simultaneously with their statistical uncertainties. The maximum likelihood function is defined as

$$\mathcal{L}(A_i, \sigma_{\mathrm{t\bar{t}}}) = \mathcal{P}(N_+^{\mathrm{obs}}, N_+^{\mathrm{pred}})\, \mathcal{P}(N_-^{\mathrm{obs}}, N_-^{\mathrm{pred}}), \tag{5}$$

where the variables $N_\pm^{\mathrm{obs}}$ and $N_\pm^{\mathrm{pred}}$ are are the respective numbers of observed and predicted events in the positive and negative regions of $\mathcal{O}_i$, and $\mathcal{P}(N_\pm^{\mathrm{obs}}, N_\pm^{\mathrm{pred}})$ denotes their Poisson probability density functions. The predicted number of events $N_\pm^{\mathrm{pred}}$ is assumed to be a function of the two fitted parameters, A_i and $\sigma_{\mathrm{t\bar{t}}}$:

$$N_\pm^{\mathrm{pred}} = N^{\mathrm{t\bar{t}}} \frac{1 \pm A_i}{2} + N^{\mathrm{bkg}} f_\pm^{\mathrm{bkg}}, \tag{6}$$

where $N^{\mathrm{t\bar{t}}} = L\mathcal{B}\varepsilon_{\mathrm{sig}}\sigma_{\mathrm{t\bar{t}}}$, with L the integrated luminosity, $\mathcal{B}$ the dileptonic branching fraction, and $\varepsilon_{\mathrm{sig}}$ the signal efficiency. The first term in Eq. (6) reflects the number of $\mathrm{t\bar{t}}$ signal events, where $N^{\mathrm{t\bar{t}}}$ includes the positive and negative regions. In the second term, N^{bkg} is the total number of events for all background processes combined, while f_+^{bkg} and f_-^{bkg} is the fraction of the number of background events in the positive (negative) regions of observable $\mathcal{O}_i$. Both f^{bkg} and N^{bkg} are fixed based on the background contributions in Table 1. Finally, the CP asymmetry and $\sigma_{\mathrm{t\bar{t}}}$ are extracted simultaneously by minimizing the negative log-likelihood function

$$-\log \mathcal{L}(A_i, \sigma_{\mathrm{t\bar{t}}}) \propto (-N_+^{\mathrm{obs}} \log N_+^{\mathrm{pred}} + N_+^{\mathrm{pred}} - N_-^{\mathrm{obs}} \log N_-^{\mathrm{pred}} + N_-^{\mathrm{pred}}). \tag{7}$$

The resulting asymmetries with their statistical uncertainties are shown in Table 2, and the extracted cross section is consistent with previous CMS results [43].

Table 2: Measured asymmetries of $\mathcal{O}_1$ and $\mathcal{O}_3$ with statistical uncertainties.

	Asymmetry and uncertainty ($\times 10^{-3}$)			
Observable	$\mathrm{e^+e^-}$	$\mathrm{e^\pm\mu^\mp}$	$\mu^+\mu^-$	Combined
$A_{\mathcal{O}_1}$	8.8 ± 7.5	0.6 ± 3.4	6.9 ± 5.3	2.4 ± 2.8
$A_{\mathcal{O}_3}$	4.1 ± 7.5	-1.7 ± 3.4	6.1 ± 5.3	0.4 ± 2.8

The asymmetries of $\mathcal{O}_1$ and $\mathcal{O}_3$ are statistically correlated, and the correlation factor is determined from pseudo-experiments to be 46%. The asymmetries measured in the three dilepton channels are combined using the best linear unbiased estimator method [45], taking into account the correlation of the systematic uncertainties across channels. A more detailed description of the combination can be found in Section 5.2.

5.2 Systematic uncertainties

Systematic uncertainties may affect the asymmetries A_i and the CEDM values. The effect of each systematic uncertainty is estimated by shifting the nominal prediction by the uncertainty and repeating the asymmetry measurement. The uncertainty is taken as the average of the absolute value of the shifts of asymmetries in the up and down directions. This allows the reduction in the statistical fluctuations in the variations. The total systematic uncertainty is calculated by adding the effect of the individual variations in quadrature. In this section, we discuss each of the sources assessed to be relevant in the analysis.

The uncertainty in the integrated luminosity determination is 2.5% [46, 47]. The uncertainty from the modeling of the number of pileup interactions is obtained by changing the inelastic pp cross section assumed in the simulation by $\pm$4.6%, consistent with the cross section uncertainty presented in Ref. [27].

The efficiencies of the triggers in data are measured as the fraction of events passing alternative triggers based on a $p_{\mathrm{T}}^{\mathrm{miss}}$ requirement that also satisfies the criteria of the trigger of interest [43, 48]. As the efficiency of the $p_{\mathrm{T}}^{\mathrm{miss}}$ requirement is only weakly correlated with the dilepton trigger efficiencies, the bias introduced by the $p_{\mathrm{T}}^{\mathrm{miss}}$ requirement is negligible. The efficiencies are close to unity in both data and simulation, as are the corresponding data-to-simulation scale factors. These scale factors are changed within their uncertainties to take into account the corresponding uncertainties in the efficiency. The scale factors for the lepton identification and isolation efficiencies are determined using a tag-and-probe method [49, 50], and the uncertainties are estimated by varying the scale factors by their uncertainties.

The calibration of the electron and muon momentum scales are varied within their uncertainties, and separately for each lepton [35, 37].

The uncertainty arising from b tagging is estimated by varying the measured b tagging scale factors within one standard deviation, depending on the p_{T} and η of the b jets [41]. The b tagging uncertainties for heavy-flavor (b and c) and light-flavor (u, d, s, and gluon) jets are calculated separately, and combined in quadrature to provide the total b tagging uncertainty.

The uncertainty arising from the jet energy scale (JES) is determined by changing the individual sources of uncertainty in the JES in bins of jet p_{T} and η, and taking their sums in quadrature [40]. These changes are then propagated to the uncertainties in $p_{\mathrm{T}}^{\mathrm{miss}}$.

An additional uncertainty in the calculation of $p_{\mathrm{T}}^{\mathrm{miss}}$ is estimated by varying the energies of reconstructed particles not clustered into jets.

The uncertainty originating from the jet energy resolution (JER) is determined by changing the JER in simulation within its uncertainty within different η regions [40].

The simulated background samples were generated with a limited number of events. Therefore, the total number of background events is affected by statistical fluctuations in these samples. The fluctuations in asymmetries originating from such limitations are evaluated through nuisance parameters in the likelihood function associated with the numbers of the background events in the negative and positive regions of the observables. The likelihood function in Eq. (5) can be modified as:

$$\mathcal{L}(A_i, \sigma_{\mathrm{t\bar{t}}}) = \mathcal{P}(N_+^{\mathrm{obs}}, N_+^{\mathrm{pred}})\, \mathcal{P}(N_-^{\mathrm{obs}}, N_-^{\mathrm{pred}})\, G(N_-^{\mathrm{bkg}}|\mu_-^{\mathrm{bkg}}, \sigma_-^{\mathrm{bkg}})\, G(N_+^{\mathrm{bkg}}|\mu_+^{\mathrm{bkg}}, \sigma_+^{\mathrm{bkg}}), \qquad (8)$$

where $\mu_\pm^{\mathrm{bkg}}$ and $\sigma_\pm^{\mathrm{bkg}}$ are the mean and the statistical uncertainty of the expected background processes. Gaussian constraints are imposed on the nuisance parameters.

The uncertainty in the normalization of the expected background processes other than $\mathrm{t\bar{t}}$ is estimated through scaling the background yield in simulation up and down by 30% [50], and then extracting the asymmetries.

The uncertainty in the PDFs used to simulate the $\mathrm{t\bar{t}}$ production is obtained using the NNPDF3.0 PDFs [51]. The impact of the uncertainty in the renormalization and factorization scale in the $\mathrm{t\bar{t}}$ simulation is estimated by varying the factorization and renormalization scales used during the generation of the simulated sample independently by factors of 0.5 and 2. The extreme cases where one scale is varied up, while the other one is varied down, are not considered.

The dependence of the asymmetries and of the CEDM on the assumed value of m_{t} is estimated by varying the generated m_{t} in the simulation by ± 1 GeV with respect to the default value of 172.5 GeV.

Previous studies have shown that the p_{T} distribution of the top quark in data is softer than expected in the NLO simulation of $\mathrm{t\bar{t}}$ production [42, 43, 52–54]. A reweighting procedure based on the p_{T} spectrum of the top quark is applied to the nominal POWHEG prediction at NLO on an event-by-event basis so as to match the simulated spectrum of the top quark p_{T} to data. The change in the result is taken as the systematic uncertainty.

The uncertainty in the b jet modeling has three components. The fragmentation into b hadrons is varied in simulation within the uncertainties of the Bowler–Lund fragmentation function tuned to ALEPH [55] and DELPHI [56] data. In addition, the difference between the Bowler–Lund [57] and the Peterson [58] fragmentation functions is included in the uncertainty. Lastly, the uncertainty from the semileptonic b hadron branching fraction is obtained by varying it by -0.45 and $+0.77$%, which is the range of the measurements from B^0/PBp decays and their uncertainties [44].

The uncertainty in the matching scale between the matrix element (ME) and the parton shower is evaluated by varying the h_{damp} parameter that regulates the emissions in POWHEG. The nominal value of h_{damp} in the simulation is $1.58m_{\mathrm{t}}$, and the modified values are $0.99m_{\mathrm{t}}$ and $2.24m_{\mathrm{t}}$, obtained from tuning the parameter using $\mathrm{t\bar{t}}$ data at $\sqrt{s} = 8$ and 13 TeV [59].

The default setup in PYTHIA includes a multiple-parton interaction (MPI) scheme of the color reconnection (CR) model with "early" resonance decays switched off. To estimate the uncertainty from this choice of model, the analysis is repeated using three other CR models within PYTHIA: the MPI-based scheme with early resonance decays switched on, a gluon-move scheme [60], and a scheme [61] inspired by quantum chromodynamics (QCD). The total uncertainty from CR modeling is estimated by taking the maximum deviation from the nominal result.

The uncertainty from modeling of the underlying event is estimated by varying the parameters that govern the underlying event modelling of the PS tune CUETP8M2T4 in Pythia8 are simultaneously varied up and down within their uncertainties [23, 59].

The renormalization scale for initial- and final-state gluon radiations (ISR and FSR) is varied up and down by a factor of 2 (for ISR) and $\sqrt{2}$ (for FSR, scaled to account for NLO compensation terms), to account for the uncertainties in the QCD scale in the parton shower description in the $\mathrm{t\bar{t}}$ simulation [23].

The observables $\mathcal{O}_1$ and $\mathcal{O}_3$ in Eqs. (2) and (3) are related to Levi-Civita tensors contracted with the four-momenta of t, $\bar{\mathrm{t}}$, b and $\bar{\mathrm{b}}$ quark jets, and two leptons. These four-momenta and the observables are affected by the uncertainties in detector measurements. A fluctuation in a measurement caused by detector response effects can change the sign of the observables in

an event, and as a consequence dilute the asymmetries. We have considered the jet angular resolutions and the charge misidentification as additional systematic sources that can dilute the asymmetries.

Jet ϕ resolution: the limited tower size of the CMS calorimeter gives rise to an uncertainty in the measured jet position. A change in the position can change the sign of an observable, leading to a change in the asymmetry. The jet ϕ information is recalculated by adding or subtracting the ϕ angle corresponding to a change by one standard deviation based on the angular resolution. Using the modified four-momenta of the jets, the observables $\mathcal{O}_1$ and $\mathcal{O}_3$ are rederived. The $\mathcal{O}_1$ and $\mathcal{O}_3$ can be recalculated using the modified four momenta of the jets.

Charge misidentification: the tracks of charged particles at high momenta become almost straight lines in the 3.8 T magnetic field. Fluctuations in the measured hit positions along the track can change the sign of the sagitta and thereby change the sign of the charged track. In such cases, the lepton charge can be misidentified, which would result in a dilution of the asymmetry. We identify two ways of misidentifying lepton charge. In the first case, the charge of one lepton is assumed to be correctly identified while the charge of the other lepton is misidentified. Since the leptons would have the same charge, events would be rejected by the $\mathrm{t\bar{t}}$ signal selection requirement of oppositely charged lepton pairs. The probability of the charge of one lepton being misidentified is calculated separately for the positive and negative region of the observables. Based on this probability, events are vetoed and the asymmetry measurements is repeated. In the second case, the charges of both leptons are assumed to be misidentified. In this case, the positions of the four-momenta of ℓ^+ and ℓ^- are swapped in the Levi-Civita tensor. Consequently, the sign of the tensor changes because of the properties of the matrix determinant. The probability that both lepton charges are misidentified is calculated separately for the positive and negative region of the observables. Assuming the worst-case scenario in which events in one of the regions contain two leptons with misidentified charge and migrate into the other region, the number of events in the regions can be re-estimated. The changes in asymmetries in the individual channels are taken as uncertainty on the asymmetry arising from charge misidentification.

In the combination, the systematic uncertainties are assumed to be fully correlated across channels, except for the uncertainty in the limited number of simulated background events and in the normalization of the background models. Since these systematic sources are statistically independent, they can be taken as uncorrelated uncertainties. The statistical uncertainties are assumed to be uncorrelated.

The dominant contributions of systematic uncertainties and additional sources are summarized in Table 3. The uncertainty is listed only if it is greater or equal than 0.4×10^{-3} for $\mathcal{O}_1$ and $\mathcal{O}_3$ in the $\mathrm{e}^{\mp}\mu^{\pm}$ channels. The uncertainties in the integrated luminosity, pileup, lepton identification and isolation, trigger, b tagging, m_{t}, top quark p_{T}, the normalization of background models, and PDFs all have small contributions and are not listed.

5.3 Extraction of CEDM

As indicated in Eq. (1), the $\mathrm{t\bar{t}}$ production vertex is modified by the presence of CEDMs, leading to CP violation. According to Ref. [8], the asymmetry defined in Eq. (4) is linearly proportional to the CEDM. Dedicated $\mathrm{t\bar{t}}$ events with such CP modifications in Eq. (1) are generated using MADGRAPH5_aMC@NLO interfaced to PYTHIA 8 [22] using the UE tune CUETP8M2.

Seven samples are generated with different values of the dimensionless CEDM $d_{\mathrm{t}G}$ parameter.

Figure 5 shows the expected asymmetries as a function of $\mathrm{Im}(d_{\mathrm{t}G})$. Within one standard devi-

Table 3: Systematic uncertainties in the measured asymmetries of $\mathcal{O}_1$ and $\mathcal{O}_3$, for the individual and combined channels.

	Uncertainty ($\times 10^{-3}$)							
	e^+e^-		$e^\mp\mu^\pm$		$\mu^+\mu^-$		Combined	
Source	$\mathcal{O}_1$	$\mathcal{O}_3$	$\mathcal{O}_1$	$\mathcal{O}_3$	$\mathcal{O}_1$	$\mathcal{O}_3$	$\mathcal{O}_1$	$\mathcal{O}_3$
Electron momentum scale/smearing	1.2	1.1	0.2	0.2	—	—	0.3	0.2
Muon momentum scale	—	—	0.1	0.2	2.3	1.0	0.5	0.3
JES	1.9	0.6	0.1	0.2	2.3	0.7	0.7	0.3
JER	2.0	0.7	0.3	0.2	1.2	0.3	0.6	0.2
Limited simulated background sample size	2.9	2.9	0.6	0.6	2.3	2.3	0.7	0.7
ME–PS matching	0.8	1.4	0.3	0.7	0.8	1.5	0.4	0.9
Color reconnection	1.9	3.8	1.6	1.0	1.0	0.9	1.5	1.1
Underlying event	0.6	0.9	1.4	1.1	1.4	1.0	1.4	1.0
ISR	1.5	1.8	0.2	0.2	0.3	0.5	0.3	0.3
FSR	1.0	1.9	0.8	0.6	0.6	0.3	0.7	0.6
Hadronization	2.0	0.5	0.6	0.3	1.7	0.2	0.9	0.3
Charge misidentification	0.8	0.8	0.4	0.4	0.1	0.1	0.3	0.3
Total systematic uncertainty	5.6	6.0	2.6	2.0	5.0	3.5	2.8	2.2

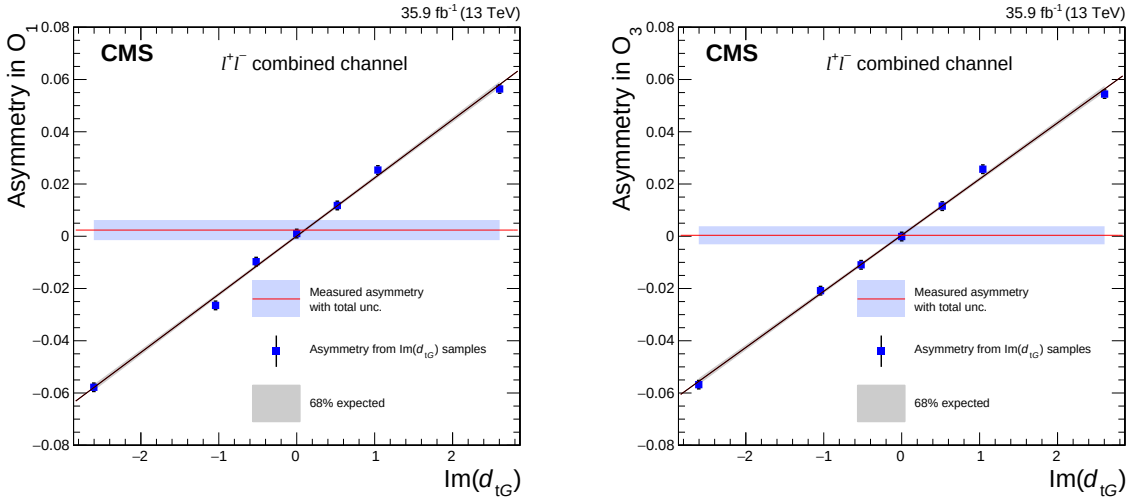

Figure 5: Asymmetries as a function of $\mathrm{Im}(d_{\mathrm{tG}})$ for $\mathcal{O}_1$ (left) and $\mathcal{O}_3$ (right), for the combined dilepton channels. The inner and outer bands correspond to the uncertainties at the 68 and 95% confidence levels, respectively, of the linear fits. The square markers are the asymmetries measured using simulated samples corresponding to the different $\mathrm{Im}(d_{\mathrm{tG}})$ values. The horizontal line indicates the measured asymmetry, and the shaded region reflects the total statistical and systematic uncertainty.

ation, the measured asymmetries are linearly proportional to the input CEDM values for both $\mathcal{O}_1$ and $\mathcal{O}_3$. The relation between the asymmetry A and the CEDM can be written as

$$A = a\,\mathrm{Im}(d_{\mathrm{tG}}) + b. \tag{9}$$

The parameters a and b are obtained from a least-squares fit to the values obtained from the

simulated samples. From this relation, $\mathrm{Im}(d_{\mathrm{t}G})$ is extracted from the measured asymmetry as

$$\mathrm{Im}(d_{\mathrm{t}G}) = \frac{A_{\mathrm{measured}} - b}{a}. \tag{10}$$

The uncertainty in the measured dimensionless CEDM $\mathrm{Im}(d_{\mathrm{t}G})$ is calculated using the full covariance matrix from the fit as

$$\Delta^2_{\mathrm{Im}(d_{\mathrm{t}G})} = \begin{pmatrix} \frac{\partial \mathrm{Im}(d_{\mathrm{t}G})}{\partial A} & \frac{\partial \mathrm{Im}(d_{\mathrm{t}G})}{\partial b} & \frac{\partial \mathrm{Im}(d_{\mathrm{t}G})}{\partial a} \end{pmatrix} \begin{pmatrix} \Delta^2_A & 0 & 0 \\ 0 & \Delta^2_b & \mathrm{cov}(b,a) \\ 0 & \mathrm{cov}(a,b) & \Delta^2_a \end{pmatrix} \begin{pmatrix} \frac{\partial \mathrm{Im}(d_{\mathrm{t}G})}{\partial A} \\ \frac{\partial \mathrm{Im}(d_{\mathrm{t}G})}{\partial b} \\ \frac{\partial \mathrm{Im}(d_{\mathrm{t}G})}{\partial a} \end{pmatrix}, \tag{11}$$

with $\Delta_{\mathrm{Im}(d_{\mathrm{t}G})}$ being the uncertainty in $\mathrm{Im}(d_{\mathrm{t}G})$, and Δ_A, Δ_a, and Δ_b the uncertainties in A, a, and b. The measured asymmetries for the combined dilepton channel are used to extract the CEDM for $\mathcal{O}_1$ and $\mathcal{O}_3$. The measured values for $\mathrm{Im}(d_{\mathrm{t}G})$ and CEDM with their statistical and systematic uncertainties are given in Table 4.

Table 4: The measured dimensionless CEDM $\mathrm{Im}(d_{\mathrm{t}G})$, extracted using the asymmetries in $\mathcal{O}_1$ and $\mathcal{O}_3$, with their uncertainties.

Observable	$\mathrm{Im}(d_{\mathrm{t}G})$
$\mathrm{A}_{\mathcal{O}_1}$	$0.10 \pm 0.12\,(\mathrm{stat}) \pm 0.12\,(\mathrm{syst})$
$\mathrm{A}_{\mathcal{O}_3}$	$0.00 \pm 0.13\,(\mathrm{stat}) \pm 0.10\,(\mathrm{syst})$

The measured asymmetries and CEDMs are consistent with the expectation from the SM of a negligible CP asymmetry. The measurement of the $\mathrm{t\bar{t}}$ spin correlation in the CMS experiment [62] also provided a CEDM value using $\hat{d}_{\mathrm{t}}$ proposed in Ref. [63]. The value $\hat{d}_{\mathrm{t}}$ from the measured $\mathrm{t\bar{t}}$ spin correlation is $-0.020 < \hat{d}_{\mathrm{t}} < 0.012$ at the 95% confidence level. The parameter $\hat{d}_{\mathrm{t}}$ is related to $\mathrm{Im}(d_{\mathrm{t}G})$ as

$$\frac{\hat{d}_{\mathrm{t}}}{m_{\mathrm{t}}} = \frac{\sqrt{2}v}{\Lambda^2}\mathrm{Im}(d_{\mathrm{t}G}). \tag{12}$$

At a new physics scale $\Lambda = 1\,\mathrm{TeV}$, using Eqs. (1) and (12), the measured $\mathrm{Im}(d_{\mathrm{t}G})$ values can be converted into $\hat{d}_{\mathrm{t}}$, resulting in $-0.014 < \hat{d}_{\mathrm{t}} < 0.027$ and $-0.019 < \hat{d}_{\mathrm{t}} < 0.019$ at the 95% confidence level, extracted from the asymmetries of $\mathcal{O}_1$ and $\mathcal{O}_3$, respectively. Hence, the sensitivity of this analysis to the CEDM $\hat{d}_{\mathrm{t}}$ value is similar to that of the $\mathrm{t\bar{t}}$ spin correlation analysis.

6 Summary

Violations of CP symmetry are studied in top quark pair production in the dilepton final state. The analysis is based on proton-proton collisions at a center-of-mass energy of 13 TeV, collected by the CMS experiment and corresponding to an integrated luminosity of $35.9\,\mathrm{fb}^{-1}$. The analysis uses two observables, $\mathcal{O}_1$ and $\mathcal{O}_3$, which are related to the Levi-Civita tensor contracted with the four-momenta of the leptons, the jets originating from the b quarks, and the top quarks. Asymmetries are measured in these observables and converted to measurements of the chromoelectric dipole moment (CEDM) of the top quark, represented by the dimensionless

CEDM $\mathrm{Im}(d_{tG})$. In the SM prediction the size of CP violation and the CEDM is negligible. The measured $\mathrm{Im}(d_{tG})$ based on the asymmetries of the $\mathcal{O}_1$ and $\mathcal{O}_3$ observables in the combined dilepton channels are $0.10 \pm 0.12\,(\mathrm{stat}) \pm 0.12\,(\mathrm{syst})$, and $0.00 \pm 0.13\,(\mathrm{stat}) \pm 0.10\,(\mathrm{syst})$, respectively. These results are consistent with the expectation of the standard model (SM), since in the SM prediction, the size of CP violation and the CEDM ($\mathrm{Im}(d_{tG})$) is negligible. In this analysis, the extracted CEDMs are compared with the CEDM measured in the $\mathrm{t\bar{t}}$ spin correlation analysis [62], and the sensitivity is found to be similar.

References

[1] J. H. Christenson, J. W. Cronin, V. L. Fitch, and R. Turlay, "Evidence for the 2π decay of the K_2^0 meson", *Phys. Rev. Lett.* **13** (1964) 138, doi:10.1103/PhysRevLett.13.138.

[2] BaBar and Belle Collaborations, "The physics of the B factories", *Eur. Phys. J. C* **74** (2014) 3026, doi:10.1140/epjc/s10052-014-3026-9, arXiv:1406.6311.

[3] LHCb Collaboration, "Observation of CP violation in charm decays", *Phys. Rev. Lett.* **122** (2019) 211803, doi:10.1103/PhysRevLett.122.211803, arXiv:1903.08726.

[4] LHCb Collaboration, "First observation of CP violation in the decays of B_s^0 mesons", *Phys. Rev. Lett.* **110** (2013) 221601, doi:10.1103/PhysRevLett.110.221601, arXiv:1304.6173.

[5] A. D. Sakharov, "Violation of CP invariance, C asymmetry, and baryon asymmetry of the universe", *Pisma Zh. Eksp. Teor. Fiz.* **5** (1967) 32, doi:10.1070/PU1991v034n05ABEH002497.

[6] G. R. Farrar and M. E. Shaposhnikov, "Baryon asymmetry of the universe in the standard model", *Phys. Rev. D* **50** (1994) 774, doi:10.1103/PhysRevD.50.774, arXiv:hep-ph/9305275.

[7] S. K. Gupta, A. S. Mete, and G. Valencia, "CP violating anomalous top-quark couplings at the LHC", *Phys. Rev. D* **80** (2009) 034013, doi:10.1103/PhysRevD.80.034013, arXiv:0905.1074.

[8] A. Hayreter and G. Valencia, "T-odd correlations from the top-quark chromoelectric dipole moment in lepton plus jets top-pair events", *Phys. Rev. D* **93** (2016) 014020, doi:10.1103/PhysRevD.93.014020, arXiv:1511.01464.

[9] D. Atwood, S. Bar-Shalom, G. Eilam, and A. Soni, "CP violation in top physics", *Phys. Rept.* **347** (2001) 1, doi:10.1016/S0370-1573(00)00112-5, arXiv:hep-ph/0006032.

[10] G. Valencia, "CP violation in top-quark pair production and decay", *PoS* **HQL2012** (2012) 050, doi:10.22323/1.166.0050, arXiv:1301.0962.

[11] CMS Collaboration, "Search for CP violation in $\mathrm{t\bar{t}}$ production and decay in proton-proton collisions at $\sqrt{s} = 8\,\mathrm{TeV}$", *JHEP* **03** (2017) 101, doi:10.1007/JHEP03(2017)101, arXiv:1611.08931.

[12] "HEPData record for this analysis", 2022. doi:10.17182/hepdata.106001.

[13] CMS Collaboration, "The CMS trigger system", *JINST* **12** (2017) P01020, doi:10.1088/1748-0221/12/01/P01020, arXiv:1609.02366.

[14] CMS Collaboration, "The CMS experiment at the CERN LHC", *JINST* **3** (2008) S08004, doi:10.1088/1748-0221/3/08/S08004.

[15] P. Nason, "A new method for combining NLO QCD with shower Monte Carlo algorithms", *JHEP* **11** (2004) 040, doi:10.1088/1126-6708/2004/11/040, arXiv:hep-ph/0409146.

[16] S. Frixione, G. Ridolfi, and P. Nason, "A positive-weight next-to-leading-order Monte Carlo for heavy flavour hadroproduction", *JHEP* **09** (2007) 126, doi:10.1088/1126-6708/2007/09/126, arXiv:0707.3088.

[17] S. Frixione, P. Nason, and C. Oleari, "Matching NLO QCD computations with parton shower simulations: the POWHEG method", *JHEP* **11** (2007) 070, doi:10.1088/1126-6708/2007/11/070, arXiv:0709.2092.

[18] S. Alioli, P. Nason, C. Oleari, and E. Re, "NLO single-top production matched with shower in POWHEG: s- and t-channel contributions", *JHEP* **09** (2009) 111, doi:10.1088/1126-6708/2009/09/111, arXiv:0907.4076. [Erratum: doi:10.1007/JHEP02(2010)011].

[19] S. Alioli, P. Nason, C. Oleari, and E. Re, "A general framework for implementing NLO calculations in shower Monte Carlo programs: the POWHEG BOX", *JHEP* **06** (2010) 043, doi:10.1007/JHEP06(2010)043, arXiv:1002.2581.

[20] E. Re, "Single-top Wt-channel production matched with parton showers using the POWHEG method", *Eur. Phys. J. C* **71** (2011) 1547, doi:10.1140/epjc/s10052-011-1547-z, arXiv:1009.2450.

[21] J. M. Campbell, R. K. Ellis, P. Nason, and E. Re, "Top-pair production and decay at NLO matched with parton showers", *JHEP* **04** (2015) 114, doi:10.1007/JHEP04(2015)114, arXiv:1412.1828.

[22] T. Sjöstrand et al., "An introduction to PYTHIA 8.2", *Comput. Phys. Commun.* **191** (2015) 159, doi:10.1016/j.cpc.2015.01.024, arXiv:1410.3012.

[23] P. Skands, S. Carrazza, and J. Rojo, "Tuning PYTHIA 8.1: the Monash 2013 tune", *Eur. Phys. J. C* **74** (2014) 3024, doi:10.1140/epjc/s10052-014-3024-y, arXiv:1404.5630.

[24] J. Alwall et al., "Comparative study of various algorithms for the merging of parton showers and matrix elements in hadronic collisions", *Eur. Phys. J. C* **53** (2008) 473, doi:10.1140/epjc/s10052-007-0490-5, arXiv:0706.2569.

[25] CMS Collaboration, "Event generator tunes obtained from underlying event and multiparton scattering measurements", *Eur. Phys. J. C* **76** (2016) 155, doi:10.1140/epjc/s10052-016-3988-x, arXiv:1512.00815.

[26] GEANT4 Collaboration, "GEANT4–a simulation toolkit", *Nucl. Instrum. Meth. A* **506** (2003) 250, doi:10.1016/S0168-9002(03)01368-8.

[27] CMS Collaboration, "Measurement of the inelastic proton-proton cross section at $\sqrt{s} = 13\,\text{TeV}$", *JHEP* **07** (2018) 161, doi:10.1007/JHEP07(2018)161, arXiv:1802.02613.

[28] K. Melnikov and F. Petriello, "Electroweak gauge boson production at hadron colliders through $O(\alpha_S^2)$", *Phys. Rev. D* **74** (2006) 114017, doi:10.1103/PhysRevD.74.114017, arXiv:hep-ph/0609070.

[29] N. Kidonakis, "NNLL threshold resummation for top-pair and single-top production", *Phys. Part. Nucl.* **45** (2014) 714, doi:10.1134/S1063779614040091, arXiv:1210.7813.

[30] J. M. Campbell and R. K. Ellis, "MCFM for the Tevatron and the LHC", *Nucl. Phys. B Proc. Suppl.* **205-206** (2010) 10, doi:10.1016/j.nuclphysbps.2010.08.011, arXiv:1007.3492.

[31] J. M. Campbell, R. K. Ellis, and C. Williams, "Vector boson pair production at the LHC", *JHEP* **07** (2011) 018, doi:10.1007/JHEP07(2011)018, arXiv:1105.0020.

[32] F. Maltoni, D. Pagani, and I. Tsinikos, "Associated production of a top-quark pair with vector bosons at NLO in QCD: impact on $t\bar{t}H$ searches at the LHC", *JHEP* **02** (2016) 113, doi:10.1007/JHEP02(2016)113, arXiv:1507.05640.

[33] M. Czakon and A. Mitov, "TOP++: A program for the calculation of the top-pair cross-section at hadron colliders", *Comput. Phys. Commun.* **185** (2014) 2930, doi:10.1016/j.cpc.2014.06.021, arXiv:1112.5675.

[34] CMS Collaboration, "Particle-flow reconstruction and global event description with the CMS detector", *JINST* **12** (2017) P10003, doi:10.1088/1748-0221/12/10/P10003, arXiv:1706.04965.

[35] CMS Collaboration, "Performance of electron reconstruction and selection with the CMS detector in proton-proton collisions at $\sqrt{s} = 8$ TeV", *JINST* **10** (2015) P06005, doi:10.1088/1748-0221/10/06/P06005, arXiv:1502.02701.

[36] CMS Collaboration, "Electron and photon performance in CMS with the full 2016 data sample", CMS Detector Performance Note CMS-DP-2017-004, 2017.

[37] CMS Collaboration, "Performance of the CMS muon detector and muon reconstruction with proton-proton collisions at $\sqrt{s} = 13$ TeV", *JINST* **13** (2018) P06015, doi:10.1088/1748-0221/13/06/P06015, arXiv:1804.04528.

[38] M. Cacciari, G. P. Salam, and G. Soyez, "The anti-k_T jet clustering algorithm", *JHEP* **04** (2008) 063, doi:10.1088/1126-6708/2008/04/063, arXiv:0802.1189.

[39] M. Cacciari, G. P. Salam, and G. Soyez, "FASTJET user manual", *Eur. Phys. J. C* **72** (2012) 1896, doi:10.1140/epjc/s10052-012-1896-2, arXiv:1111.6097.

[40] CMS Collaboration, "Jet energy scale and resolution in the CMS experiment in pp collisions at 8 TeV", *JINST* **12** (2017) P02014, doi:10.1088/1748-0221/12/02/P02014, arXiv:1607.03663.

[41] CMS Collaboration, "Identification of heavy-flavour jets with the CMS detector in pp collisions at 13 TeV", *JINST* **13** (2018) P05011, doi:10.1088/1748-0221/13/05/P05011, arXiv:1712.07158.

[42] CMS Collaboration, "Measurement of the differential cross section for top quark pair production in pp collisions at $\sqrt{s} = 8$ TeV", *Eur. Phys. J. C* **75** (2015) 542, doi:10.1140/epjc/s10052-015-3709-x, arXiv:1505.04480.

[43] CMS Collaboration, "Measurements of $\mathrm{t\bar{t}}$ differential cross sections in proton-proton collisions at $\sqrt{s} = 13\,\text{TeV}$ using events containing two leptons", *JHEP* **02** (2019) 149, doi:10.1007/JHEP02(2019)149, arXiv:1811.06625.

[44] Particle Data Group, P. A. Zyla et al., "Review of particle physics", *Prog. Theor. Exp. Phys.* **2020** (2020) 083C01, doi:10.1093/ptep/ptaa104.

[45] L. Lyons, D. Gibaut, and P. Clifford, "How to combine correlated estimates of a single physical quantity", *Nucl. Instrum. Meth. A* **270** (1988) 110, doi:10.1016/0168-9002(88)90018-6.

[46] CMS Collaboration, "CMS luminosity measurements for the 2016 data-taking period", CMS Physics Analysis Summary CMS-PAS-LUM-17-001, 2017.

[47] CMS Collaboration, "Precision luminosity measurement in proton-proton collisions at $\sqrt{s} = 13\,\text{TeV}$ in 2015 and 2016 at CMS", *Eur. Phys. J. C* **81** (2021) 800, doi:10.1140/epjc/s10052-021-09538-2, arXiv:2104.01927.

[48] CMS Collaboration, "Measurement of the $\mathrm{t\bar{t}}$ production cross section, the top quark mass, and the strong coupling constant using dilepton events in pp collisions at $\sqrt{s} = 13\,\text{TeV}$", *Eur. Phys. J. C* **79** (2019) 368, doi:10.1140/epjc/s10052-019-6863-8, arXiv:1812.10505.

[49] CMS Collaboration, "Measurement of the Drell–Yan cross sections in pp collisions at $\sqrt{s} = 7$ TeV with the CMS experiment", *JHEP* **10** (2011) 007, doi:10.1007/JHEP10(2011)007, arXiv:1108.0566.

[50] CMS Collaboration, "Measurement of the top quark pair production cross section in proton-proton collisions at $\sqrt{s} = 13\,\text{TeV}$ with the CMS detector", *Phys. Rev. Lett.* **116** (2016) 052002, doi:10.1103/PhysRevLett.116.052002, arXiv:1510.05302.

[51] J. Butterworth et al., "PDF4LHC recommendations for LHC Run II", *J. Phys. G* **43** (2016) 023001, doi:10.1088/0954-3899/43/2/023001, arXiv:1510.03865.

[52] CMS Collaboration, "Measurement of differential top-quark pair production cross sections in pp collisions at $\sqrt{s} = 7\,\text{TeV}$", *Eur. Phys. J. C* **73** (2013) 2339, doi:10.1140/epjc/s10052-013-2339-4, arXiv:1211.2220.

[53] CMS Collaboration, "Measurement of the $\mathrm{t\bar{t}}$ production cross section in the all-jets final state in pp collisions at $\sqrt{s} = 8\,\text{TeV}$", *Eur. Phys. J. C* **76** (2016) 128, doi:10.1140/epjc/s10052-016-3956-5, arXiv:1509.06076.

[54] CMS Collaboration, "Measurement of differential cross sections for top quark pair production using the lepton+jets final state in proton-proton collisions at 13 TeV", *Phys. Rev. D* **95** (2017) 092001, doi:10.1103/PhysRevD.95.092001, arXiv:1610.04191.

[55] ALEPH Collaboration, "Study of the fragmentation of b quarks into B mesons at the Z peak", *Phys. Lett. B* **512** (2001) 30, doi:10.1016/S0370-2693(01)00690-6, arXiv:hep-ex/0106051.

[56] DELPHI Collaboration, "A study of the b-quark fragmentation function with the DELPHI detector at LEP I and an averaged distribution obtained at the Z pole", *Eur. Phys. J. C* **71** (2011) 1557, doi:10.1140/epjc/s10052-011-1557-x, arXiv:1102.4748.

[57] M. G. Bowler, "e^+e^- production of heavy quarks in the string model", *Z. Phys. C* **11** (1981) 169, doi:10.1007/BF01574001.

[58] C. Peterson, D. Schlatter, I. Schmitt, and P. M. Zerwas, "Scaling violations in inclusive e^+e^- annihilation spectra", *Phys. Rev. D* **27** (1983) 105, doi:10.1103/PhysRevD.27.105.

[59] CMS Collaboration, "Investigations of the impact of the parton shower tuning in PYTHIA 8 in the modelling of $t\bar{t}$ at $\sqrt{s} = 8$ and 13 TeV", CMS Physics Analysis Summary CMS-PAS-TOP-16-021, 2016.

[60] S. Argyropoulos and T. Sjöstrand, "Effects of color reconnection on $t\bar{t}$ final states at the LHC", *JHEP* **11** (2014) 043, doi:10.1007/JHEP11(2014)043, arXiv:1407.6653.

[61] J. R. Christiansen and P. Z. Skands, "String formation beyond leading colour", *JHEP* **08** (2015) 003, doi:10.1007/JHEP08(2015)003, arXiv:1505.01681.

[62] CMS Collaboration, "Measurement of the top quark polarization and $t\bar{t}$ spin correlations using dilepton final states in proton-proton collisions at $\sqrt{s} = 13$ TeV", *Phys. Rev. D* **100** (2019) 072002, doi:10.1103/PhysRevD.100.072002, arXiv:1907.03729.

[63] W. Bernreuther, D. Heisler, and Z.-G. Si, "A set of top quark spin correlation and polarization observables for the LHC: Standard model predictions and new physics contributions", *JHEP* **12** (2015) 026, doi:10.1007/JHEP12(2015)026, arXiv:1508.05271.